

A High-Field EPR Study of the Accelerated Dynamics of the Amorphous Fraction of Semicrystalline Poly(dimethylsiloxane) at the Melting Point

Carlo Andrea Massa · Silvia Pizzanelli ·
Vasile Bercu · Luca Pardi · Monica Bertoldo ·
Dino Leporini

Received: 9 June 2014 / Revised: 13 June 2014 / Published online: 27 June 2014
© Springer-Verlag Wien 2014

Abstract The reorientation of a small paramagnetic tracer in poly(dimethylsiloxane) (PDMS) has been investigated by high-field electron paramagnetic resonance spectroscopy at a Larmor frequency of 285 GHz. The tracer is confined in the disordered phase of the semicrystalline PDMS. A sudden change of the rotational dynamics is observed close to the melting point (213 K) of the crystallites. This points to strong coupling between the crystalline and the disordered fractions of PDMS. Below the glass transition ($T_g \sim 150\text{K}$), the tracer reorientation occurs via small angle jumps, with no apparent distribution of the correlation times. Above T_g , a power-law distribution of correlation times is evidenced.

C. A. Massa · L. Pardi · M. Bertoldo · D. Leporini
Istituto per i Processi Chimico-Fisici-Consiglio Nazionale delle Ricerche (IPCF-CNR),
via G. Moruzzi 1, 56124 Pisa, Italy

C. A. Massa
e-mail: carlo.andrea.massa@pi.ipcf.cnr.it

S. Pizzanelli
Istituto di Chimica dei Composti Organometallici-Consiglio Nazionale
delle Ricerche (ICCOM-CNR), via G. Moruzzi 1, 56124 Pisa, Italy

V. Bercu
Department of Physics, University of Bucharest, Str. Atomistilor 405,
Magurele, Jud. Ilfov, 077125 Bucharest, Romania

D. Leporini (✉)
Dipartimento di Fisica “Enrico Fermi”, Università di Pisa,
Largo B. Pontecorvo 3, 56127 Pisa, Italy
e-mail: leporini@df.unipi.it

1 Introduction

In a semicrystalline polymer (SCP), the macromolecules pack together in ordered regions called crystallites which are separated by disordered regions [1]. In fact, due to the severe constraints of the connectivity, ordering in SCPs is very rarely complete. The disordered domains are amorphous solids below the glass transition temperature T_g , whereas on heating and crossing T_g , they gain increased mobility and transform to rubbers or viscoelastic liquids. By further heating, crystallites melt. Melting first involves the smallest crystallites, whereas thicker and more ordered ones become unstable at higher temperatures. Above the melting temperature, if the polymeric chains are not cross-linked, molecular flow is possible.

Relaxation processes in SCPs are complicated. If relaxation below T_g is hardly sensitive to crystallization due to the very local character, above T_g the viscoelastic liquid is largely affected by the confinement due to the presence of the crystallites. This is particularly apparent in the elastic properties of SPCs in that they tend to form very tough plastics because of the strong intermolecular forces associated with close chain packing in the crystallites. It is seen that below T_g the elastic modulus of SCPs depends weakly on the crystallinity, whereas above T_g the increase of the degree of crystallinity enhances the modulus [1, 2]. Furthermore, transport properties, such as diffusion and permeability, are also markedly affected by the crystallinity degree since the crystallites are very often impermeable even to small molecules which are expelled by the ordered regions during the crystallization [2–4]. Notice that such a phenomenon is well known to chemists, who commonly use crystallization as a purification technique.

The confinement of small tracer molecules in the disordered fraction offers the possibility of selective studies of such regions in semicrystalline materials. One viable approach is provided by electron paramagnetic resonance (EPR) which is able to investigate the reorientation of spin probes, such as nitroxide molecules, dissolved in the host matrix of interest at very low concentration ($\lesssim 1$ mM) [5]. EPR investigations of polymeric materials using spin probes are widely reported [6–11]. Use of spin probes in semicrystalline materials is reported in ice–water mixtures [12–17] whereas, as far as we know, it is quite limited in SCPs [18, 19]. It is worth noting that EPR studies of irradiated SCPs are quite common, especially to study fracture [20, 21]. However, this approach is unable to discriminate in an easy and reliable way the contributions to the overall signal coming from the crystalline and the disordered fractions of SCPs. This drawback is shared with several other techniques usually used in the investigation of polymeric materials, e.g. NMR, dielectric relaxation, neutron scattering.

Here, we demonstrate the technique of using spin probe in SCPs in a study of poly(dimethylsiloxane) (PDMS) by means of high-field electron paramagnetic resonance (HF EPR) spectroscopy at a Larmor frequency of 285 GHz. The strong influence of the melting of the crystalline fraction on the disordered one is evidenced. This is completely different from what is observed in polycrystalline ice, where spin probes confined in intergranular water are unable to detect ice melting [15–17]. This points to the conclusion that the disordered and the ordered fraction in SCPs are more strongly coupled, most probably due to the connectivity.

2 Materials and Methods

2.1 Sample

2,2,6,6-Tetramethyl-1-piperidinyloxy (TEMPO) paramagnetic tracer and PDMS, characterized by a weight-average molecular weight (Mw) of 90,200 g/mol and by a polydispersity (Mw/Mn) of 1.96, were purchased from Aldrich and used as received. The sample was prepared by dissolving TEMPO and PDMS in chloroform according to the solution method [22]. Then, the solution was heated at about 330 K for 24 h and no residual chloroform was detected by NMR. TEMPO concentration was <0.04 % in weight. The sample (about 0.5 cm³) was put in a Teflon holder, which was then placed in a single-pass probe cell. Differential scanning calorimetry (DSC) analysis, performed on a Seiko SII Exstar DSC 7020 calorimeter, equipped with liquid nitrogen cooling unit, at a heating rate of 3 K/min after a cooling scan at the same rate, gave the following transitions: $T_g = 147\text{K}$, cold crystallization at 183 K, and melting onset at about 209 K with endothermic peaks at 228 and 234 K. For similar systems, the crystallinity fraction was found to be 0.3–0.4 [23, 24].

2.2 EPR Measurements and Lineshape Analysis

The EPR measurements were carried out on the ultrawideband EPR spectrometer detailed elsewhere [25]. The spectrometer was operated at 285 GHz. The sample was cooled in situ from room temperature to 124 K at an average rate of 1 K/min and spectra were recorded stepwise at increasing temperatures. In these conditions, when the glass transition is reached, crystallization should be complete, according to the crystallization rates reported in the literature for similar systems [23, 24, 26, 27]. The sample was kept about one hour at each temperature before the measurement.

TEMPO has one unpaired electron with spin $S = 1/2$ subject to hyperfine coupling to ¹⁴N nucleus with spin $I = 1$. For the calculation of the lineshapes, we used numerical routines described elsewhere [28]. The \mathbf{g} and hyperfine \mathbf{A} tensor interactions were considered and assumed to have the same principal axes. The x axis is parallel to the N–O bond, the z axis is parallel to the nitrogen and oxygen 2π orbitals, and the y axis is perpendicular to the other two. The principal components of the two tensors (g_{xx} , g_{yy} , g_{zz} , A_{xx} , A_{yy} and A_{zz}) are input parameters to calculate the EPR lineshape. They were carefully measured by simulating the “powder” spectrum, i. e. that recorded at very low temperature, where the lineshape is not influenced by the tracer reorientation (Fig. 1). A_{xx} and A_{yy} values are affected by a large uncertainty because they are small compared to the linewidth. To obtain more reliable values, we used the additional constraint $\frac{1}{3}(A_{xx} + A_{yy} + A_{zz}) = A_{\text{iso}}$, with A_{iso} being the hyperfine splitting observed in the melt at 280 K and assumed that $A_{xx} = A_{yy}$. The best-fit magnetic parameters, which were not adjusted in the simulations of the HF EPR signal, are $g_{xx} = 2.0095$, $g_{yy} = 2.0058$, $g_{zz} = 2.0017$, $A_{xx} = 0.47$ mT, $A_{yy} = 0.47$ mT and $A_{zz} = 3.40$ mT.

The tracer rotation is assumed to occur by sudden jumps of angular width ϵ_0 around isotropically distributed rotation axes after a mean residence time τ^* in each orientation. The corresponding rotational correlation time τ (the area below the

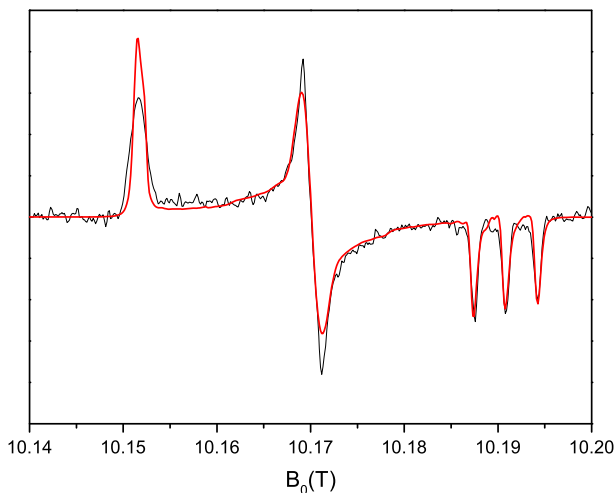


Fig. 1 Experimental (*black line*) and simulated (*red line*) HF EPR spectra at 285 GHz of TEMPO in PDMS at 124 K (color figure online)

correlation function of the spherical harmonic $Y_{2,0}$ is $\tau^*/[1 - \sin(5\epsilon_0/2)/(5\sin(\epsilon_0/2))]$ [29, 30]. In the presence of jump dynamics, τ^* and τ do not differ too much, hence τ may be identified with the waiting time before an activated jump takes place [30–36].

The theoretical lineshape was convoluted with a Gaussian function with a width of 0.1 mT to account for the residual broadening.

The spectra in the presence of a distribution of correlation times $\rho(\tau)$ were calculated by summing up about 150 spectra characterized by correlation times in the range 0.003–165 ns, each spectrum being weighted according to the distribution parameters. The best-fit parameters and the related uncertainties were obtained by routine procedures. Only two parameters were adjusted at most, as it will be detailed below.

3 Results and Discussion

3.1 EPR Lineshapes

Figure 2 shows selected first-derivative HF EPR spectra at 285 GHz of TEMPO in PDMS in the temperature range 124–280 K. The spectra markedly change with the temperature above $T_g = 147$ K. In particular, one notices that the changes are quite apparent also at lower temperatures than the melting onset at about 209 K. This is consistent with the expectation that TEMPO is mostly dissolved in the disordered fraction of PDMS.

The lineshape at 124 K is that expected for a “powder” sample, independent of the rotational dynamics (see Sect. 2.2). As the temperature is increased, the

difference between the resonating magnetic fields of the outermost peaks ΔB (see Fig. 2) decreases and the linewidth of the peaks increases, until the features reminding those of the “powder” sample are lost around 211 K. Above that temperature, the motional narrowing of the EPR lineshape becomes strong and a triplet structure starts appearing, which is more and more sharpening as the temperature is increased. It should be noticed that the appearance of the three-peak pattern mentioned above occurs in a very narrow temperature range (about 3 K), suggesting a dramatic increase of the rotational rate of the spin probe.

Figure 3 plots the quantity ΔB (see Fig. 2) and the average linewidth of the three outermost lines on the right hand side of the spectra in the glass transition region. Both quantities signal the increasing mobility of TEMPO above the glass transition. The linewidth increases with the temperature. The decrease of ΔB with the temperature is comparable to that observed in other polymers [11]. Neither ΔB nor the width shows any discontinuity at T_g .

3.2 Molecular Motion: Single Correlation Time and Distribution of Correlation Times

To gain quantitative information on the tracer dynamics, we adopted the jump model described in Sect. 2.2, which depends on the adjustable parameters ϵ_0 and τ , the jump angular width and the correlation time, respectively. Initially, dynamical homogeneity is assumed, namely the reorientation of all the TEMPO molecules is accounted for by a single correlation time. This will be referred to as single correlation time (SCT) model.

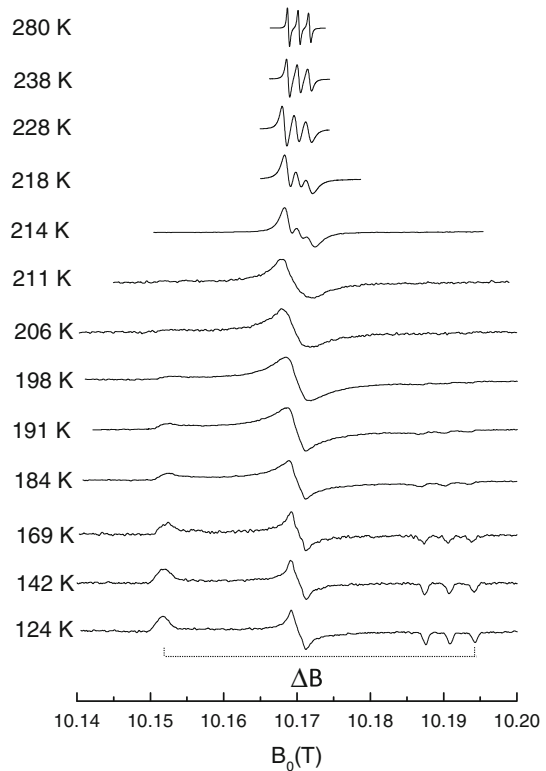
The spectra below $T_g \sim 150\text{K}$ were successfully simulated using the SCT model. At such slow rotational rates, the lineshape is weakly sensitive to the jump angle size. In fact, the quality of the simulation does not change if ϵ_0 spans the range of 5° – 20° . On the other hand, the remarkable change of ΔB with temperature, shown in Fig. 3, rules out that the jump angle size ϵ_0 is large [10]. Henceforth, with the purpose of limiting the number of adjustable parameters, one sets $\epsilon_0 = 10^\circ$. Figure 4 proves the effectiveness of the SCT model below T_g . The small discrepancy between the simulation and the peak at low magnetic field was already noted [11].

In the temperature region above T_g , the SCT model is rather poor. This is exemplified in Fig. 5, showing a comparison with the experimental spectrum at 189 K. In fact, it is known that polymeric materials exhibit heterogeneous dynamics above T_g [6–8]. Then, the assumption of a single correlation time for all the TEMPO molecules is not justified. Therefore, we considered the EPR lineshape $L(B_0)$ as a weighted superposition of contributions:

$$L(B_0) = \int_0^{\infty} L(B_0, \tau) \rho(\tau) d\tau, \quad (1)$$

where $L(B_0, \tau)$ and $\rho(\tau)$ are the EPR lineshape of the spin probes with correlation time τ and the distribution of correlation times, respectively. To get an adequate

Fig. 2 HF EPR spectra at 285 GHz of TEMPO in PDMS at selected temperatures. ΔB is the difference between the resonating magnetic fields of the outermost peaks observed at lower temperatures



form of $\rho(\tau)$, some alternatives were compared. First, we considered the log-Gauss distribution (LGD):

$$\rho_{\text{LGD}}(\tau) = \frac{1}{\sqrt{2\pi\sigma^2}} \exp\left[-\frac{1}{2\sigma^2} \left(\ln \frac{\tau}{\tau_{\text{LGD}}}\right)^2\right] \frac{1}{\tau}, \quad (2)$$

which depends on the two adjustable parameters τ_{LGD} and σ . This distribution implies a Gaussian distribution of barrier heights and was employed in EPR [8], NMR [37] and quasi-elastic neutron scattering studies [38, 39]. Figure 5 shows the spectrum calculated using LGD at 189 K. The linewidth of the three outermost lines at high field is clearly overestimated and marked deviations are observed at about 10.17 T.

As an alternative, we employed the power-law distribution (PD) [9–11]:

$$\rho_{\text{PD}}(\tau) = \begin{cases} 0 & \text{if } \tau < \tau_{\text{PD}} \\ x \cdot \tau_{\text{PD}}^x \cdot \tau^{-(x+1)} & \text{if } \tau \geq \tau_{\text{PD}}, \end{cases} \quad (3)$$

τ_{PD} and x are the shortest correlation time and a width parameter, respectively. Such a distribution significantly improves the simulation, as shown in Fig. 5. A similar analysis was repeated at the other temperatures and led us to the conclusion to adopt the PD model. Notice that the PD model yields the SCT model in the limit $x \gg 1$. It

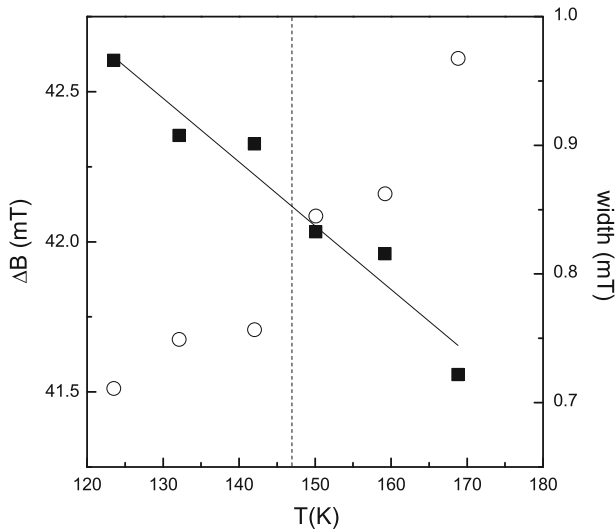


Fig. 3 Temperature dependence of the quantity ΔB (see Fig. 2 for definition) and the linewidth of the three outermost lines on the *right-hand side* of the spectra (*filled squares* and *empty circles*, respectively). The superimposed line is the linear fit $\Delta B = a + bT$, with $a = 45 \pm 0.27$ mT and $b = -0.0211 \pm 0.0018$ mT/K. The *vertical dashed line* marks the glass transition temperature

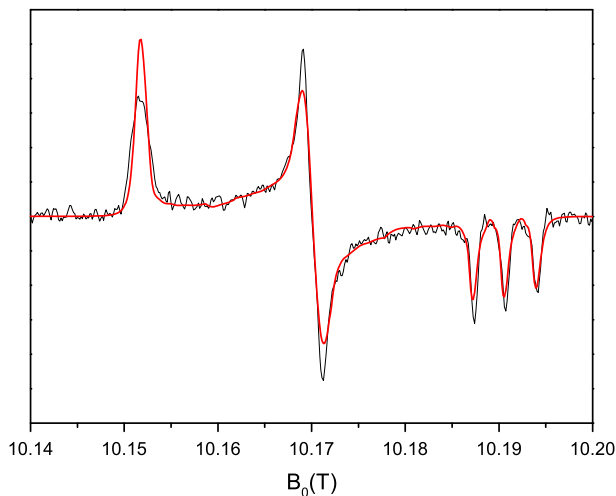


Fig. 4 Experimental (*black line*) and simulated (*red line*) HF EPR spectra at 285 GHz of TEMPO in PDMS at 142 K. The simulation was performed using the SCT model with $\tau_{\text{SCT}} = 80$ ns and jump angle $\epsilon_0 = 10^\circ$ (color figure online)

is worth noting that the PD model interprets the width parameter as $x = kB\overline{E}$ where kB and \overline{E} are the Boltzmann constant and the average energy barrier, respectively [9]. Thus, on increasing the temperature, x increases and the PD

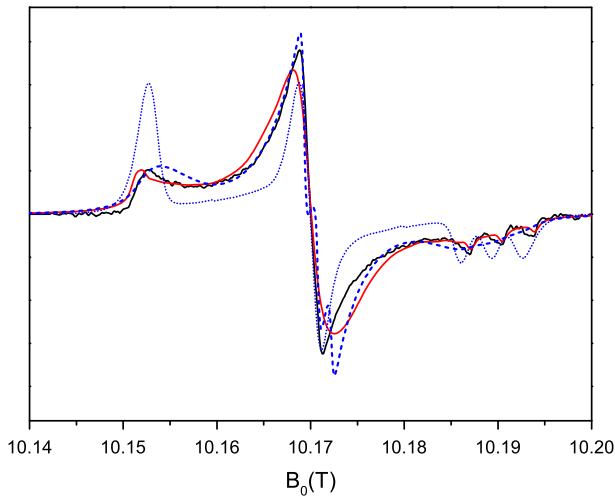


Fig. 5 Experimental HF EPR spectrum of TEMPO in PDMS at 189 K (black line) compared to spectra calculated using SCT (blue short dot line), LGD (blue short dashed line) and PD (red solid line) models. The dynamic parameters used are: $\tau_{\text{SCT}} = 12$ ns, $\tau_{\text{LGD}} = 1.0$ ns, $\sigma = 1.3$ and $\tau_{\text{PD}} = 0.14$ ns and $x = 0.45$ (color figure online)

distribution narrows. This is expected due to the more effective average of the local surroundings of TEMPO by the faster host fluctuations.

Figure 6 shows a comparison of the experimental and the calculated lineshapes at different temperatures above T_g using the PD model or its SCT limit at the higher temperatures. A nice agreement with the experimental spectra is observed. The use of the SCT model at higher temperatures follows by the fact that the x width parameter of the PD model increases with the temperature. The decreasing difference between the PD and SCT models on increasing the temperature is shown in Fig. 7.

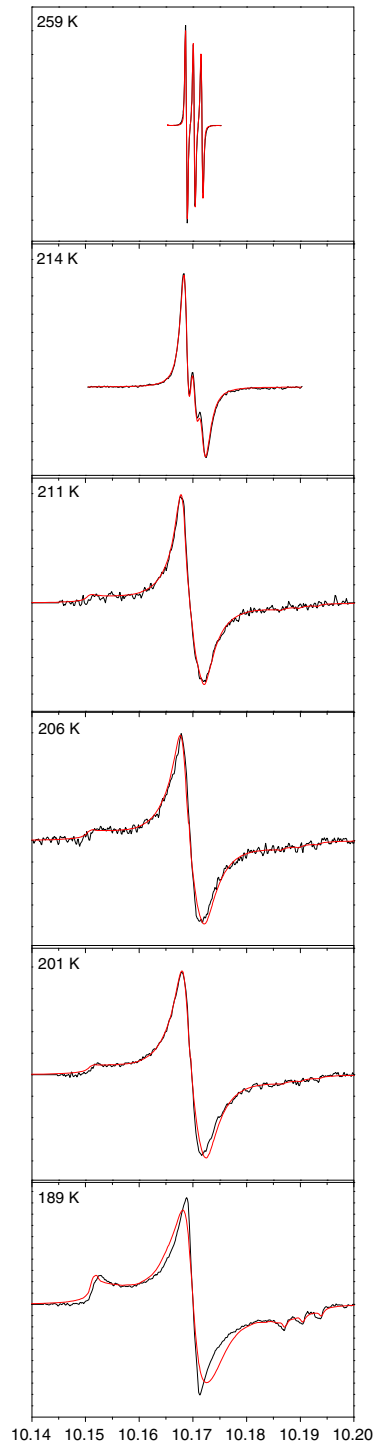
3.3 Temperature Dependence of the Average Rotational Correlation Time $\langle\tau\rangle$ and Distribution Width

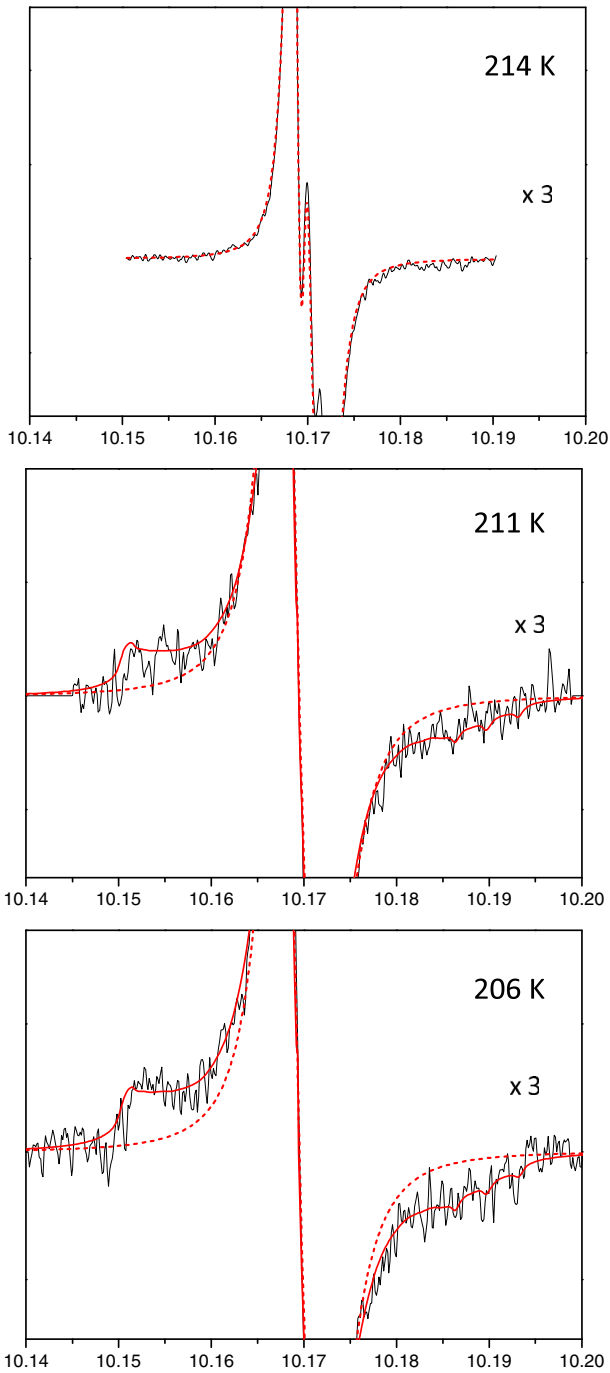
A proper account of the reorientation of TEMPO is provided by the average reorientation time $\langle\tau\rangle$:

$$\langle\tau\rangle = \int_0^{\infty} \tau \rho_{\text{PD}}(\tau) d\tau. \quad (4)$$

Figure 8 shows that $\langle\tau\rangle$ decreases with the temperature, with no anomaly at the glass transition. This indicates that the probe dynamics is decoupled from the structural relaxation of the disordered fraction, which is too slow to be detected by EPR. For temperatures below 180 K, the temperature dependence of $\langle\tau\rangle$ is described by an Arrhenius law, with an activation energy of 3.5 ± 0.4 kJ/mol. A close value, 4.6 kJ/mol, was found for PDMS investigated by quasi-elastic neutron scattering in the

Fig. 6 Experimental (*black line*) and simulated (*red line*) HF EPR spectra of TEMPO in PDMS at different temperatures above T_g . The simulations are performed by the PD model apart from the two higher temperatures where the SCT model is used. The best-fit parameters are (from *bottom to top*): $x = 0.45$ and $\tau_{PD} = 0.14$ ns; $x = 0.63$ and $\tau_{PD} = 0.10$ ns; $x = 0.70$ and $\tau_{PD} = 0.10$ ns; $x = 0.75$ and $\tau_{PD} = 0.08$ ns; $\tau_{SCT} = 0.06$ ns; $\tau_{SCT} = 0.007$ ns





◀ **Fig. 7** Experimental (black) and simulated (red solid line and red dashed line for PD and SCT model, respectively) spectra in the temperature region close to the melting of PDMS crystallites. The simulation parameters are: at 214 K, $\tau_{\text{SCT}} = 0.065$ ns; at 211 K, $\tau_{\text{SCT}} = 0.15$ ns and $\tau_{\text{PD}} = 0.08$ ns, $x = 0.75$; at 206 K, $\tau_{\text{SCT}} = 0.15$ ns and $\tau_{\text{PD}} = 0.10$ ns, $x = 0.70$

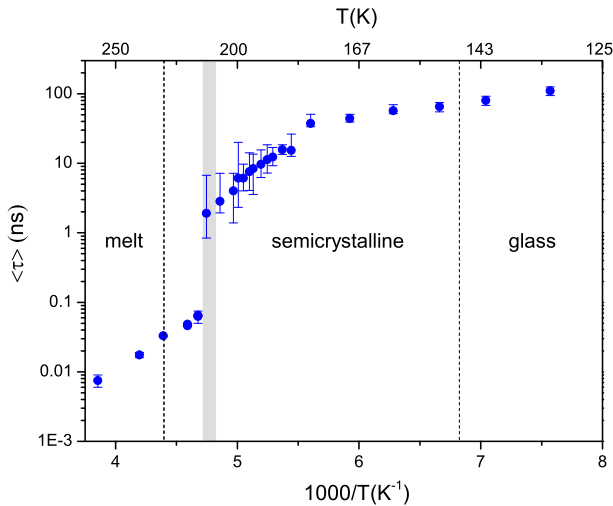


Fig. 8 Temperature dependence of $\langle \tau \rangle$ derived from Eq. 4 and the best-fit parameters of the spectral simulations

range 100–200 K and attributed to CH_3 reorientation [38] thus suggesting a good coupling between the probe and local motions.

At about 213 K, where the EPR lineshape exhibits a dramatic change (see Fig. 2), a steep decrease of $\langle \tau \rangle$ by about one order of magnitude is found. At this temperature, the polymer starts melting according to DSC measurements. We speculate that the chains of the amorphous phase tethered to the crystal fronts and/or restricted by the crystal lamellas increase their mobility at the melt of the ordered domains. As a result, the reorientation rate of the spin probe, which is located in the amorphous phase, speeds up.

The temperature dependence of $\langle \tau \rangle$ of TEMPO in the PDMS melt is described by an Arrhenius law, with an activation energy of 18.8 ± 0.9 kJ/mol, which is comparable to 14.6 kJ/mol observed for PDMS segmental dynamics [38]. It is worth noting that, differently from lower temperatures, a much stronger coupling to the structural relaxation is now observed which is ascribed to the similarity of the time scales of the relaxation and the TEMPO reorientation. Notice that the cooperative nature of the structural relaxation yields a larger activation energy of the TEMPO reorientation in the PDMS melt with respect to the one observed close to T_g ascribed to the coupling between TEMPO and local processes.

The temperature dependence of the width parameter x , as drawn by the best-fit procedure, is shown in Fig. 9. The x parameter shows a smooth increase with the

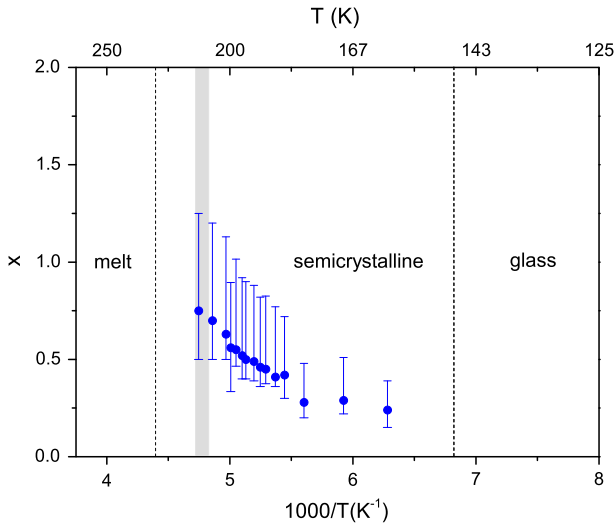


Fig. 9 Temperature dependence of the width parameter of the PD distribution, Eq. 3. The *dashed vertical lines* mark the glass and the melt transition temperatures, while the *grey area* identifies the region of the melting onset

temperature. The subsequent narrowing of $\rho_{\text{PD}}(\tau)$, Eq. 3, at high temperature is in qualitative agreement with both the remarks in Sect. 3.2 concerning the PD model and other relaxation models [40]. Above 213 K, x is much larger than 1, and the PD model approaches the SCT limit.

It seems proper to point out the difference between the narrowing of $\rho_{\text{PD}}(\tau)$ at high temperature and the apparent narrowing observed below 159 K, see Sect. 3.2. The latter is not due to a change in the dynamical heterogeneity as at high temperature, but to the finite range of correlation times accessible to EPR. In fact, on decreasing the temperature, the correlation times increase, approaching the longest value detectable by EPR ($\sim 0.1 \mu\text{s}$). As a consequence, an increasingly larger part of the actual distribution of the reorientation times of TEMPO in PDMS yields a nearly identical powder-like spectrum. This results in an apparent narrowing of the distribution.

4 Conclusions

The reorientation of TEMPO confined in the disordered fraction of the semi-crystalline PDMS has been investigated by HF EPR. Below T_g , the tracer reorientation occurs via small angle jumps, with no apparent distribution of the correlation times, whereas above T_g a power-law distribution of correlation times is evidenced. On increasing the temperature, the distribution narrows. Evidence of the accelerated dynamics of TEMPO at the melting point of the crystallites is given. The results suggest that the crystalline and the disordered fractions of

PDMS are strongly coupled, in contrast with the case of ice–water mixtures where spin probes dissolved in water do not detect melting. This suggests the strong role by the chain connectivity. The reorientation of TEMPO close to T_g is limited by local processes and weakly coupled to the structural relaxation. Instead, TEMPO is more strongly coupled to the cooperative structural relaxation of the PDMS melt.

References

1. U.W. Gedde, *Polymer Physics* (Chapman and Hall, London, 1995)
2. M. Cocca, M.L.D. Lorenzo, M. Malinconico, V. Frezza, *Eur. Polym. J.* **47**, 1073 (2011)
3. M. Driessens, R. Peeters, J. Mullens, D. Franco, P.J. Lemstra, D.G. Hristova-Bogaerds, *J. Polym. Sci. Part B Polym. Phys.* **47**, 2247 (2009)
4. S.C. George, S. Thomas, *Prog. Polym. Sci.* **26**, 985 (2001)
5. L.J. Berliner, J. Reuben (eds.), *Biological Magnetic Resonance* (Plenum, New York, 1989)
6. G.G. Cameron, in *Comprehensive Polymer Science*, ed. by C. Booth, C. Price (Pergamon, Oxford, 1989)
7. B. Rånby, J. Rabek, *ESR Spectroscopy in Polymer Research* (Springer, Berlin, 1977)
8. M. Faetti, M. Giordano, D. Leporini, L. Pardi, *Macromolecules* **32**, 1876 (1999)
9. V. Bercu, M. Martinelli, C.A. Massa, L.A. Pardi, D. Leporini, *J. Phys. Condens. Matter* **16**, L479 (2004)
10. V. Bercu, M. Martinelli, L. Pardi, C.A. Massa, D. Leporini, *Z. Phys. Chemie* **226**, 1379 (2012)
11. V. Bercu, M. Martinelli, C.A. Massa, L.A. Pardi, D. Leporini, *J. Chem. Phys.* **123**, 174906 (2005)
12. R. Ross, *J. Chem. Phys.* **42**, 3919 (1965)
13. J.L. Jr., G. Reed, *J. Phys. Chem.* **75**, 1202 (1971)
14. M.K. Ahn, *J. Chem. Phys.* **64**, 134 (1976)
15. D. Banerjee, S.N. Bhat, S.V. Bhat, D. Leporini, *Proc. Natl. Acad. Sci. USA* **106**, 11448 (2009)
16. D. Banerjee, S.N. Bhat, S.V. Bhat, D. Leporini, *PLOS One* **7**, e44382 (2012)
17. D. Banerjee, S.V. Bhat, D. Leporini, *Adv. Chem. Phys.* **152**, 1 (2013)
18. M.M. Dorio, J.C.W. Chien, *Macromolecules* **8**, 734 (1975)
19. S. Kutsumizu, M. Goto, S. Yano, *Macromolecules* **37**, 4821 (2004)
20. M.S. Jahan, in *UHMWPE Biomaterials Handbook*, ed. by S.M. Kurtz (Academic Press, London, 2009), pp. 433–450
21. K. Makuuchi, S. Cheng, *Radiation Processing of Polymer Materials and Its Industrial Applications* (Wiley, Hoboken, 2012)
22. J.W. Saalmueller, H.W. Long, T. Volkmer, U. Wiesner, G.G. Maresch, H.W. Spiess, *J. Polym. Sci. Pt. B-Polym. Phys.* **34**(6), 1093 (1996)
23. R. Lund, A. Alegría, L. Goitandía, J. Colmenero, M.A. González, P. Lindner, *Macromolecules* **41**(4), 1364 (2008)
24. R.H. Ebengou, J.P. Cohen-Addad, *Polymer* **35**(14), 2962 (1994)
25. L.C. Brunel, A. Caneschi, A. Dei, D. Friselli, D. Gatteschi, A.K. Hassan, L. Lenci, M. Martinelli, C.A. Massa, L.A. Pardi, F. Popescu, I. Ricci, L. Sorace, *Res. Chem. Intermed.* **28**(2–3), 215 (2002)
26. A. Maus, K. Saalwächter, *Macromol. Chem. Phys.* **208**(19–20), 2066 (2007)
27. M.I. Aranguren, *Polymer* **39**(20), 4897 (1998)
28. M. Giordano, P. Grigolini, D. Leporini, P. Marin, *Phys. Rev. A* **28**(4), 2474 (1983)
29. E.N. Ivanov, *Sov. Phys. JETP* **18**(4), 1041 (1964)
30. L. Andreozzi, F. Cianflone, C. Donati, D. Leporini, *J. Phys. Condens. Matter* **8**, 3795 (1996)
31. A. Ottochian, D. Leporini, *J. Non. Cryst. Solids* **357**, 298 (2011)
32. A. Ottochian, C. De Michele, D. Leporini, *J. Chem. Phys.* **131**, 224517 (2009)
33. L. Andreozzi, M. Giordano, D. Leporini, *J. Non-Cryst. Solids* **235**, 219 (1998)
34. L. Larini, A. Barbieri, D. Prevosto, P.A. Rolla, D. Leporini, *J. Phys. Condens. Matter* **17**, L199 (2005)
35. A. Barbieri, G. Gorini, D. Leporini, *Phys. Rev. E* **69**, 061509 (2004)

36. F. Puosi, D. Leporini, *J. Chem. Phys.* **136**, 041104 (2012)
37. C. Schmidt, K.J. Kuhn, H.W. Spiess, *Prog. Colloid Polym. Sci.* **71**, 71 (1985)
38. V. Arrighi, S. Gagliardi, C. Zhang, F. Ganazzoli, J.S. Higgins, R. Ocone, M.T.F. Telling, *Macromolecules* **36**(23), 8738 (2003)
39. A. Chahid, A. Alegria, J. Colmenero, *Macromolecules* **27**(12), 3282 (1994)
40. N.V. Surovtsev, J.A.H. Wiedersich, V.N. Novikov, E. Rössler, A.P. Sokolov, *Phys. Rev. B* **58**(22), 14888 (1998)